ADVANCED ENERGY MATERIALS

Supporting Information

for *Adv. Energy Mater.,* DOI: 10.1002/aenm.202002861

Operando EDXRD Study of All-Solid-State Lithium Batteries Coupling Thioantimonate Superionic Conductors with Metal Sulfide

Xiao Sun, Alyssa M. Stavola, Daxian Cao, Andrea M. Bruck, Ying Wang, Yunlu Zhang, Pengcheng Luan, Joshua W. Gallaway, and Hongli Zhu**

Supporting Information

Operando EDXRD Study of All-solid-state Lithium Batteries Coupling Thioantimonate Superionic Conductors with Metal Sulfide

Xiao Sun[1,&], Alyssa M. Stavola[2,&], Daxian Cao[1,&], Andrea M. Bruck[2], Ying Wang[1], Yunlu Zhang[1], Pengcheng Luan[1], Joshua W. Gallaway[2,*], Hongli Zhu[1,*]

[1]Department of Mechanical and Industrial Engineering, Northeastern University, 360 Huntington Avenue, Boston, Massachusetts, 02115, United States

[2]Department of Chemical Engineering, Northeastern University, 360 Huntington Avenue, Boston, Massachusetts, 02115, United States

*: Correspondence: h.zhu@neu.edu (H. Z.), j.gallaway@northeastern.edu (J. W. G.)

1. XRD patterns of $Li_{6+x}Ge_xSb_{1-x}S_5I$ (x=0.2, 0.4, 0.6, 0.8)

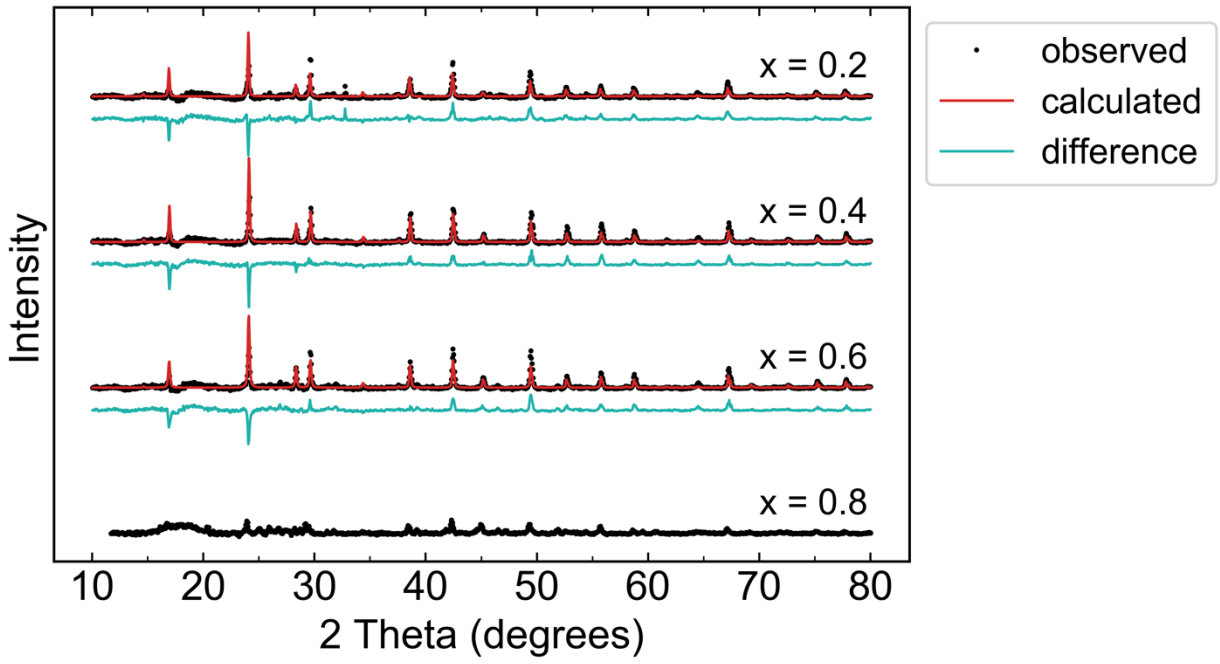

Figure S1. *XRD patterns of $Li_{6+x}Ge_xSb_{1-x}S_5I$ where x was 0.2, 0.4, 0.6, and 0.8, respectively. All of the patterns have been background corrected. Three of the patterns are displayed with Rietveld refinements (x = 0.2, 0.4, 0.6) to the F-43m space group.*

The Rietveld refinements to the XRD patterns use the structural model provided by Zhou et al.[1] Their demonstration of the Li3(48h) occupancy increase creating vacancies on the Li1(48h)−Li2(24g)−Li1(48h) equilibrium sites was hypothesized to account for the superionic conductivity of the substituted materials with $x \geq 0.5$. They established this using neutron powder diffraction. While they used neutron powder diffraction to resolve the four Li positions, our model limited Li occupancy to the 48h Li1 site due to limited Li scattering using X-ray diffraction.[2] For this reason, our refinement method confined Li occupancy to the Ge occupancy. Zhou et al. demonstrated that Li occupancy has limited effect on the refined structure, making this method valid. This provided structural validation of the values of x in our synthesized materials.

Table S1 displays the refined stoichiometry of $Li_{6+x}Ge_xSb_{1-x}S_5I$ for x = 0.2, 0.4, and 0.6, which are within error of the reported values. Table S2-S4 demonstrate the crystallographic parameters for $Li_{6+x}Ge_xSb_{1-x}S_5I$ with x = 0.2, 0.4, and 0.6 respectively.

Table S1: Refined Stoichiometry from Rietveld Refinements with weighted residuals values. Refined values of x are determined using the Ge atom occupancy.

Theoretical x	Refined x	Refined Stoichiometry	wR
0.6	0.63±0.06	$Li_{6.62(6)}Ge_{0.63(6)}Sb_{0.37(6)}S_5I$	6.9%
0.4	0.42±0.06	$Li_{6.43(6)}Ge_{0.42(6)}Sb_{0.58(6)}S_5I$	6.7%
0.2	0.2±0.1	$Li_{6.2(1)}Ge_{0.2(1)}Sb_{0.8(1)}S_5I$	6.8%

Table S2: Crystallographic parameters for $Li_{6+x}Ge_xSb_{1-x}S_5I$ where x = 0.2 with space group F-43m. Refinement is shown in Figure S1.

Atom	**Wyckoff site**	**x**	**y**	**z**	**occupancy**
Li	48h	0.28(1)	0.50(2)	0.78(1)	0.517(9)
Ge	4b	0.5	0.5	0.5	0.2(1)
Sb	4b	0.5	0.5	0.5	0.8(1)
S1	4c	0.25	0.25	0.25	0.976
S2	16e	0.362(1)	0.362(1)	0.638(1)	1
S3	4a	0.5	0.5	0	0.024
I1	4a	0.5	0.5	0	0.976
I2	4c	0.25	0.25	0.25	0.024

Table S3: Crystallographic parameters for $Li_{6+x}Ge_xSb_{1-x}S_5I$ where x = 0.4 with space group F-43m. Refinement is shown in Figure S1.

Atom	Wyckoff site	x	y	z	occupancy
Li	48h	0.28(1)	0.51(2)	0.78(1)	0.535(5)
Ge	4b	0.5	0.5	0.5	0.42(6)
Sb	4b	0.5	0.5	0.5	0.58(6)
S1	4c	0.25	0.25	0.25	0.976
S2	16e	0.362(1)	0.362(1)	0.638(1)	1
S3	4a	0.5	0.5	0	0.024
I1	4a	0.5	0.5	0	0.977
I2	4c	0.25	0.25	0.25	0.023

Table S4: Crystallographic parameters for $Li_{6+x}Ge_xSb_{1-x}S_5I$ where x = 0.6 with space group F-43m. Refinement shown in Figure S1.

Atom	Wyckoff site	x	y	z	occupancy
Li	48h	0.27(2)	0.54(1)	0.77(2)	0.552(5)
Ge	4b	0.5	0.5	0.5	0.63(6)
Sb	4b	0.5	0.5	0.5	0.37(6)
S1	4c	0.25	0.25	0.25	0.976
S2	16e	0.363(1)	0.363(1)	0.637(1)	1
S3	4a	0.5	0.5	0	0.024
I1	4a	0.5	0.5	0	0.976
I2	4c	0.25	0.25	0.25	0.024

2. SEM images of $Li_{6.6}Ge_{0.6}Sb_{0.4}S_5I$

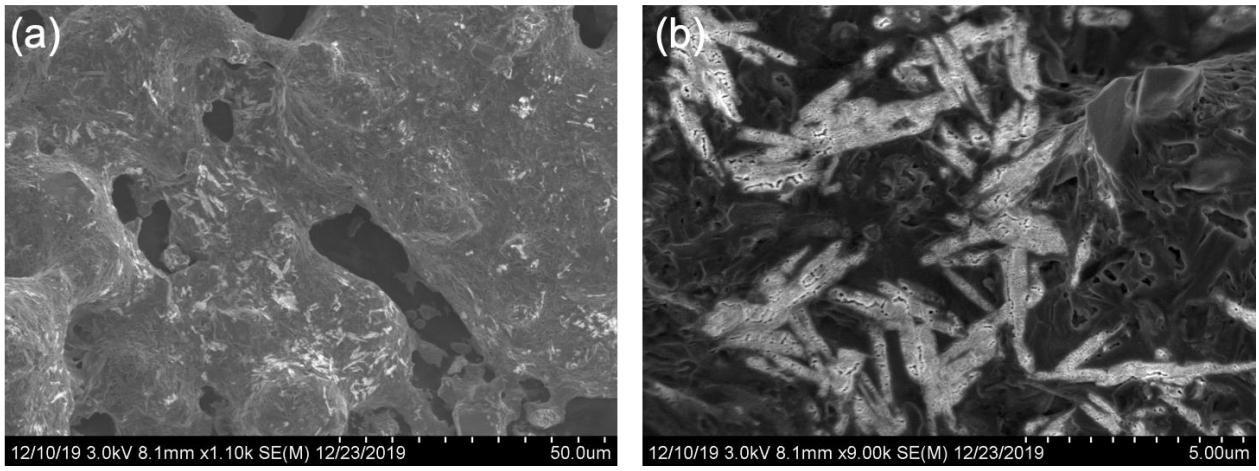

***Figure S2**. SEM images of $Li_{6.6}Ge_{0.6}Sb_{0.4}S_5I$ at (a) low and (b) high magnification.*

3. Ionic conductivities of $Li_{6+x}Ge_xSb_{1-x}S_5I$ (x=0.2, 0.4, 0.6, 0.8)

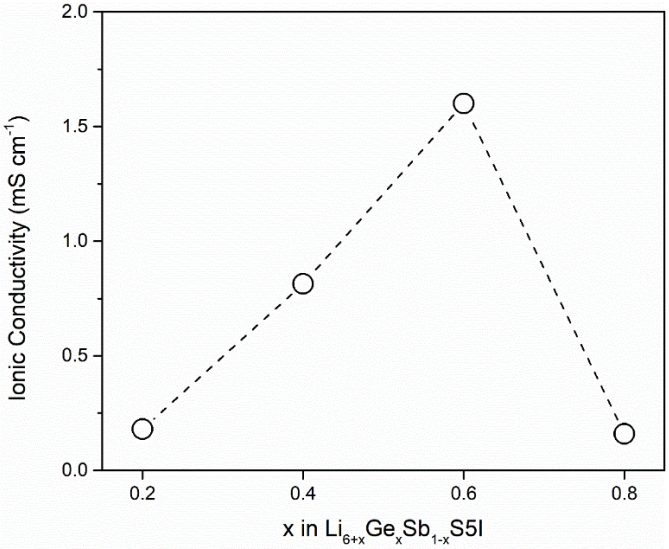

Figure S3*. Ionic conductivities of $Li_{6+x}Ge_xSb_{1-x}S_5I$ where x was 0.2, 0.4, 0.6, and 0.8, respectively.*

4. Ionic conductivity of $Li_{6.6}Ge_{0.6}Sb_{0.4}S_5I$ at different temperature

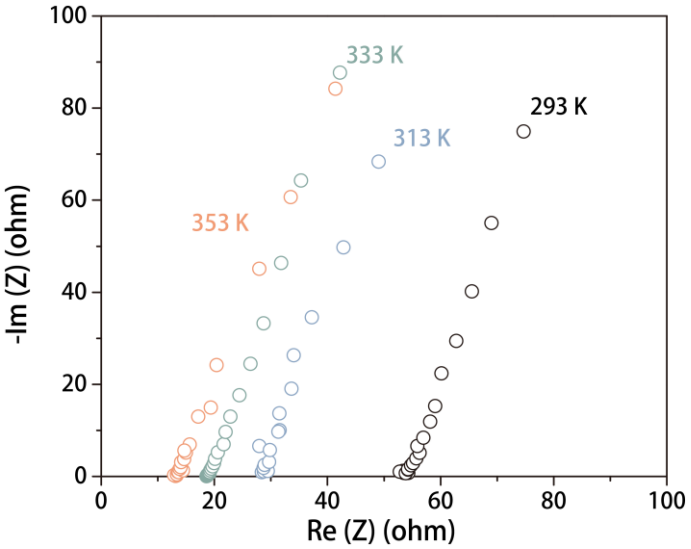

Figure S4. *EIS data showing ionic conductivity of* $Li_{6.6}Ge_{0.6}Sb_{0.4}S_5I$ *at 20, 40, 60, and 80 ℃, respectively*.

5. Air stability measurement

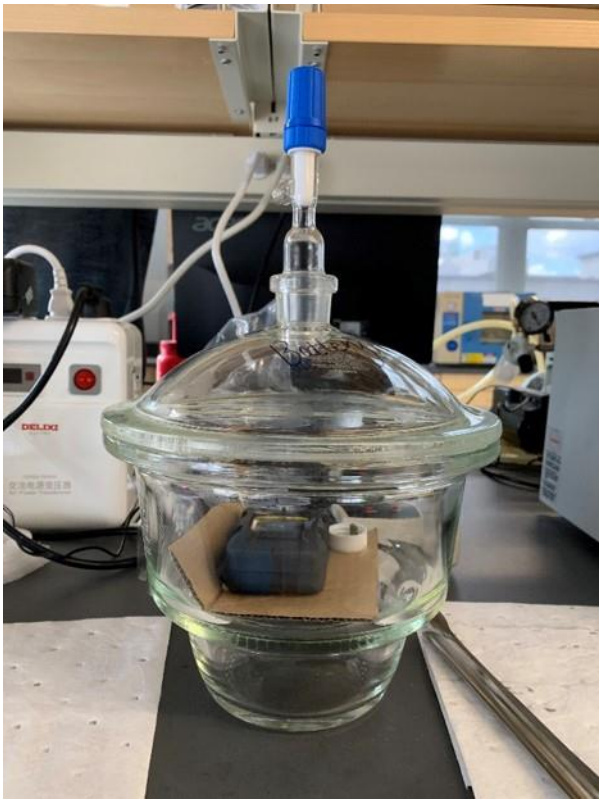

Figure S5*. Photo of the desiccator used to measure the air stability of solid electrolytes. The* H_2S *sensor was placed inside the desiccator.*

6. Ionic conductivity measurement.

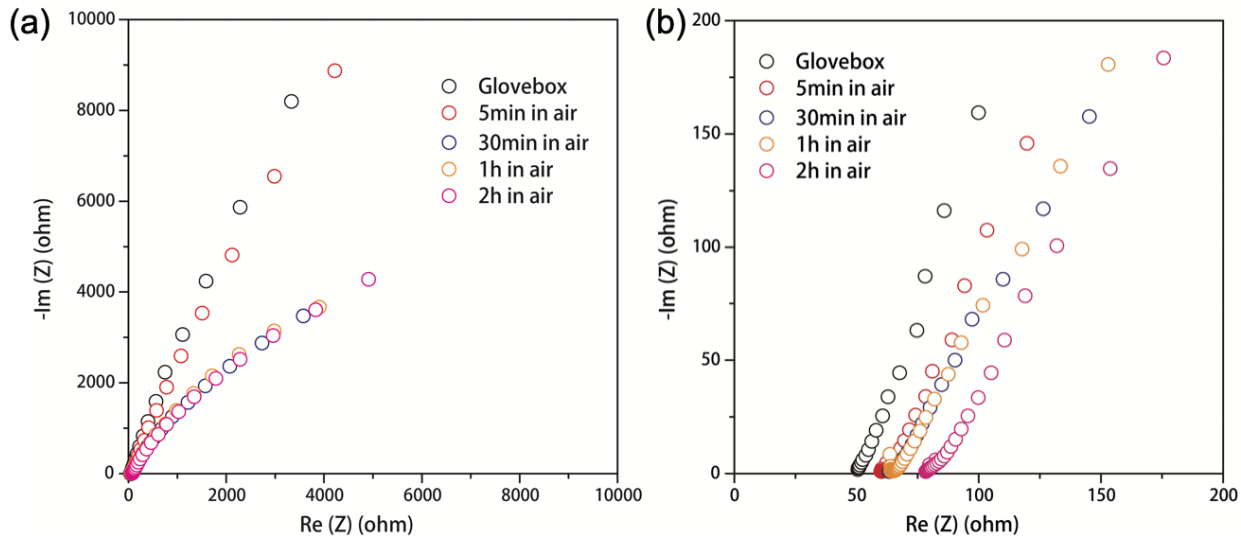

Figure S6. (a)The Nyquist plots of LGSSI when exposed to air for a different time. (b) Zoom-in image to show the impedance evolution.

7. Linear sweep voltammetry (LSV) measurement in $Li_{6.6}Ge_{0.6}Sb_{0.4}S_5I$ /C | $Li_{6.6}Ge_{0.6}Sb_{0.4}S_5I$ | Li-In

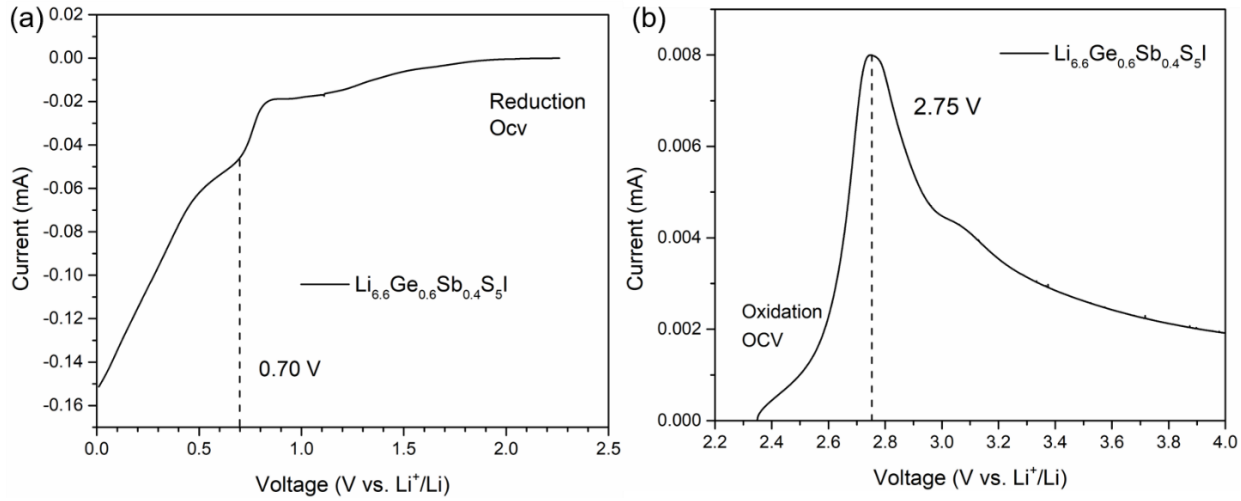

Figure S7*. LSV profiles of $Li_{6.6}Ge_{0.6}Sb_{0.4}S_5I$ /C | $Li_{6.6}Ge_{0.6}Sb_{0.4}S_5I$ | Li cells that without adding a liquid electrolyte to evaluate the electrochemical stability of $Li_{6.6}Ge_{0.6}Sb_{0.4}S_5I$ (a) during reduction at low voltage (OCV to 0.0 V) and (b) during oxidation at high voltage (OCV to 4.0 V).*

8. Linear sweep voltammetry measurement in $Li_{6.6}Ge_{0.6}Sb_{0.4}S_5I$ /C | $Li_{6.6}Ge_{0.6}Sb_{0.4}S_5I$ | Li-In

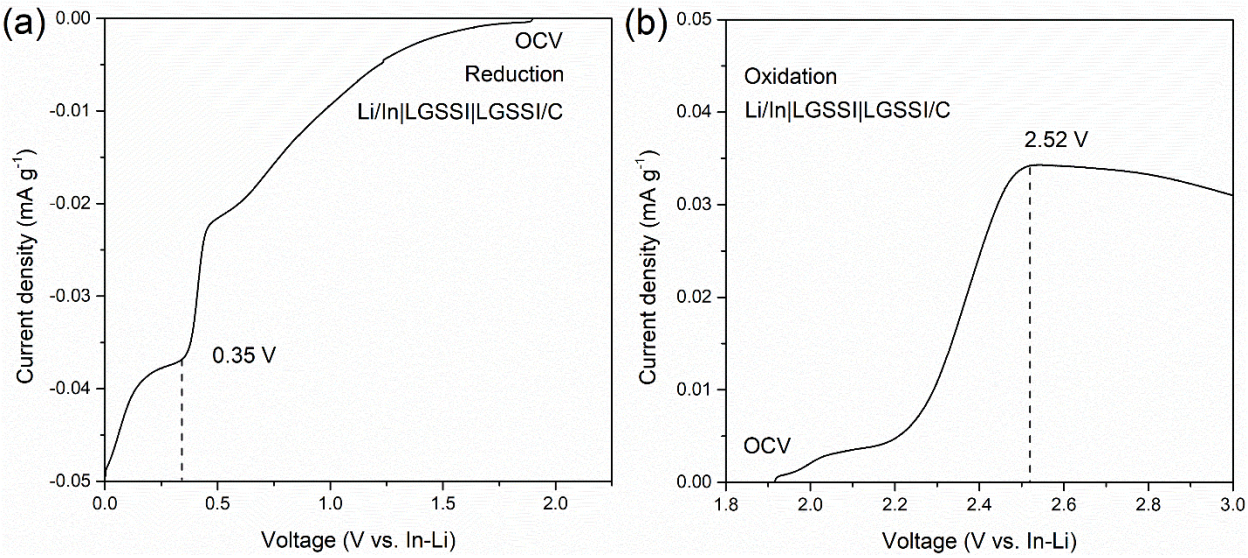

Figure S8*. LSV profiles of $Li_{6.6}Ge_{0.6}Sb_{0.4}S_5I$ /C | $Li_{6.6}Ge_{0.6}Sb_{0.4}S_5I$ | Li-In cell to evaluate the electrochemical stability of $Li_{6.6}Ge_{0.6}Sb_{0.4}S_5I$ (a) during reduction at low voltage (OCV to 0.0 V) and (b) during oxidation at high voltage (OCV to 3.0 V).*

9. Initial EDXRD data for the $Li_{6.6}Ge_{0.6}Sb_{0.4}S_5I$ /C | $Li_{6.6}Ge_{0.6}Sb_{0.4}S_5I$ | Li-In cell tested by LSV from OCV to 0 V

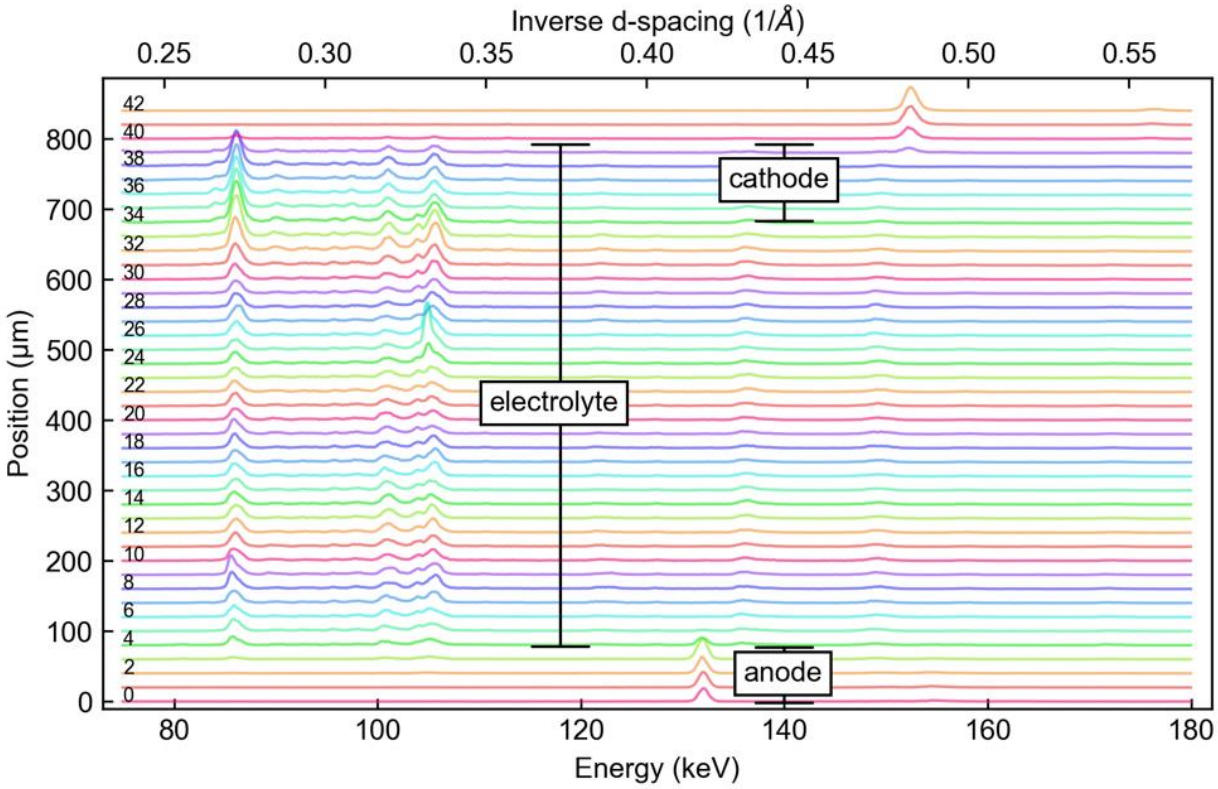

***Figure S9**. Initial EDXRD data for the $Li_{6.6}Ge_{0.6}Sb_{0.4}S_5I$ /C | $Li_{6.6}Ge_{0.6}Sb_{0.4}S_5I$ | Li-In cell tested by LSV from OCV to 0 V at time 1, with locations of each scan from 0 - 42 marked with the corresponding position in the cell in µm. This data is the same as is plotted in Figure 4b, but here it is plotted as individual diffraction patterns.*

10. EDXRD data for all times during reduction in the $Li_{6.6}Ge_{0.6}Sb_{0.4}S_5I$ /C | $Li_{6.6}Ge_{0.6}Sb_{0.4}S_5I$ | Li-In cell shown in Figure 4d of the main text.

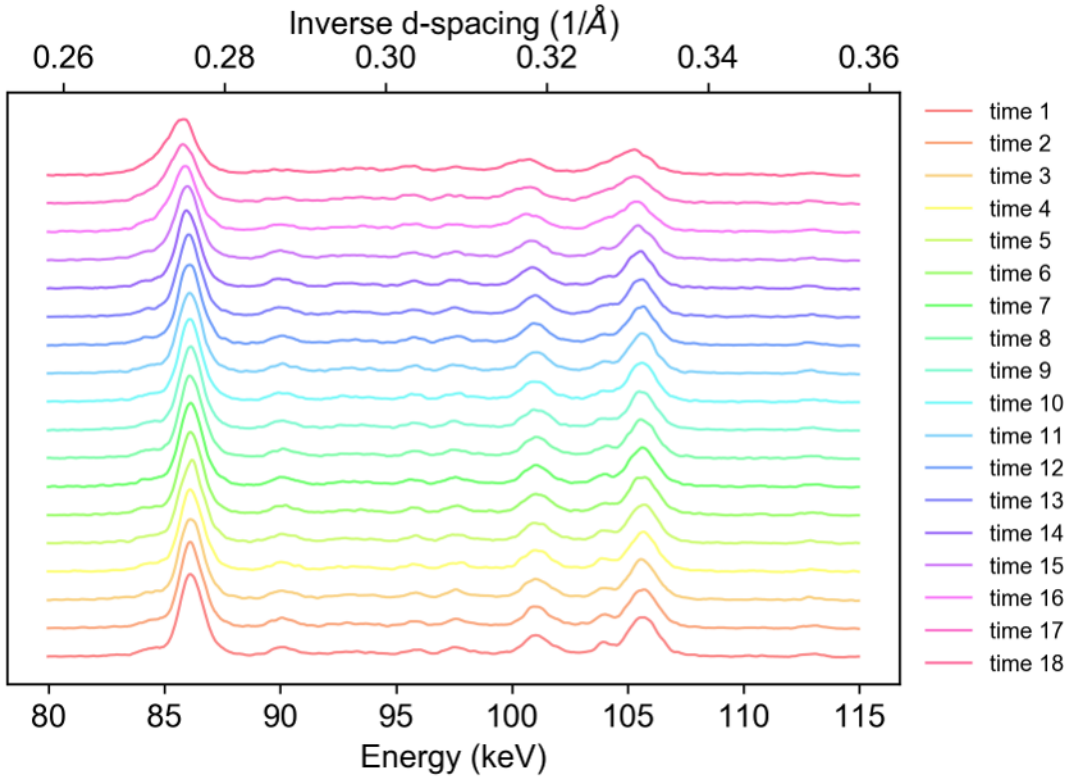

Figure S10. *EDXRD data for the $Li_{6.6}Ge_{0.6}Sb_{0.4}S_5I$ /C | $Li_{6.6}Ge_{0.6}Sb_{0.4}S_5I$ | Li-In cell tested by LSV from OCV to 0 V, shown from 80-115 keV for all times at location 34. This is the full time series from Figure 4d in the main text.*

11. Initial EDXRD data for the $Li_{6.6}Ge_{0.6}Sb_{0.4}S_5I$ /C | $Li_{6.6}Ge_{0.6}Sb_{0.4}S_5I$ | Li-In cell tested by LSV from OCV to 3 V

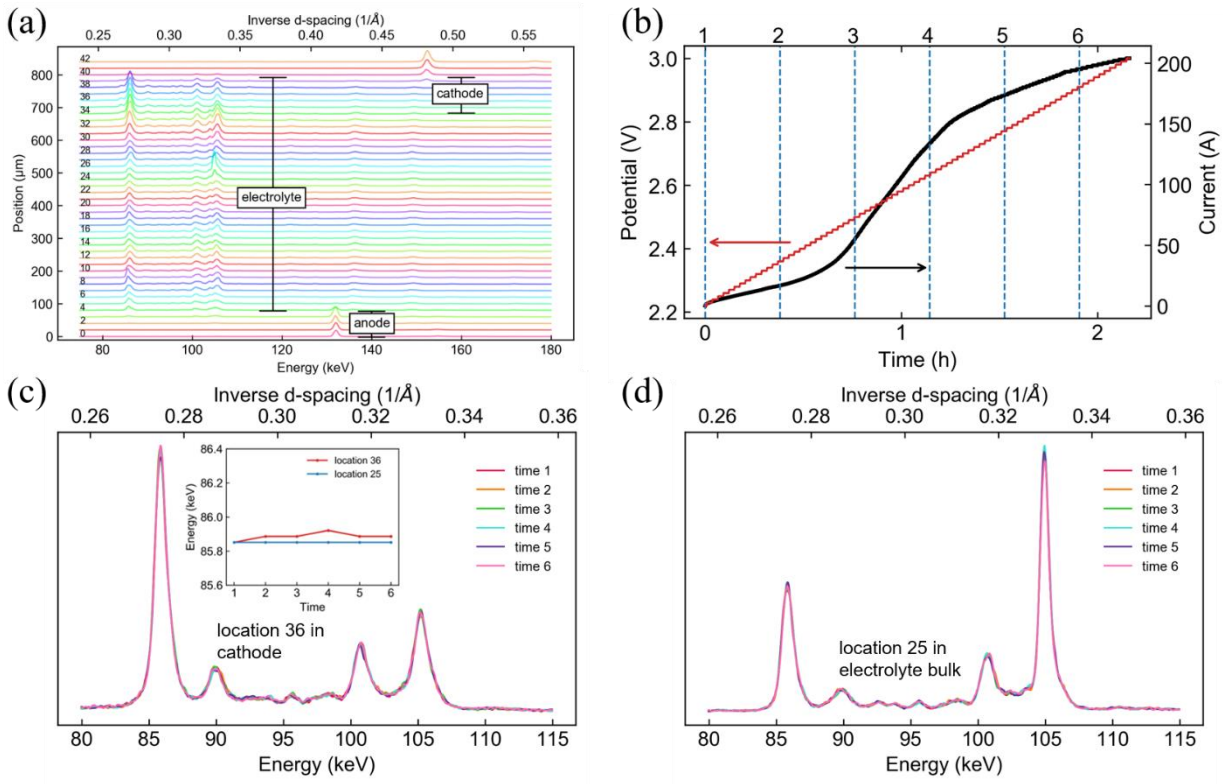

Figure S11. *(a) initial EDXRD data for the second $Li_{6.6}Ge_{0.6}Sb_{0.4}S_5I$ /C | $Li_{6.6}Ge_{0.6}Sb_{0.4}S_5I$ | Li-In cell tested by LSV from OCV to 3 V (time 1). (b) Times where scans were taken during linear sweep voltammetry with potential (red) and current (black) also displayed. Major $Li_{6.6}Ge_{0.6}Sb_{0.4}S_5I$ peaks as a function of time in a half cell at (c) location 36 in the carbon black cathode and (d) location 25 in the electrolyte bulk. Both locations show no significant crystalline changes of $Li_{6.6}Ge_{0.6}Sb_{0.4}S_5I$. Inset shows the energy of the $Li_{6.6}Ge_{0.6}Sb_{0.4}S_5I$ (220) reflection in the cathode (red) versus the bulk SE layer (blue).*

12. Initial EDXRD data of pristine FeS_2/C/ $Li_{6.6}Ge_{0.6}Sb_{0.4}S_5I$ | $Li_{6.6}Ge_{0.6}Sb_{0.4}S_5I$ | Li-In full cell (time 1)

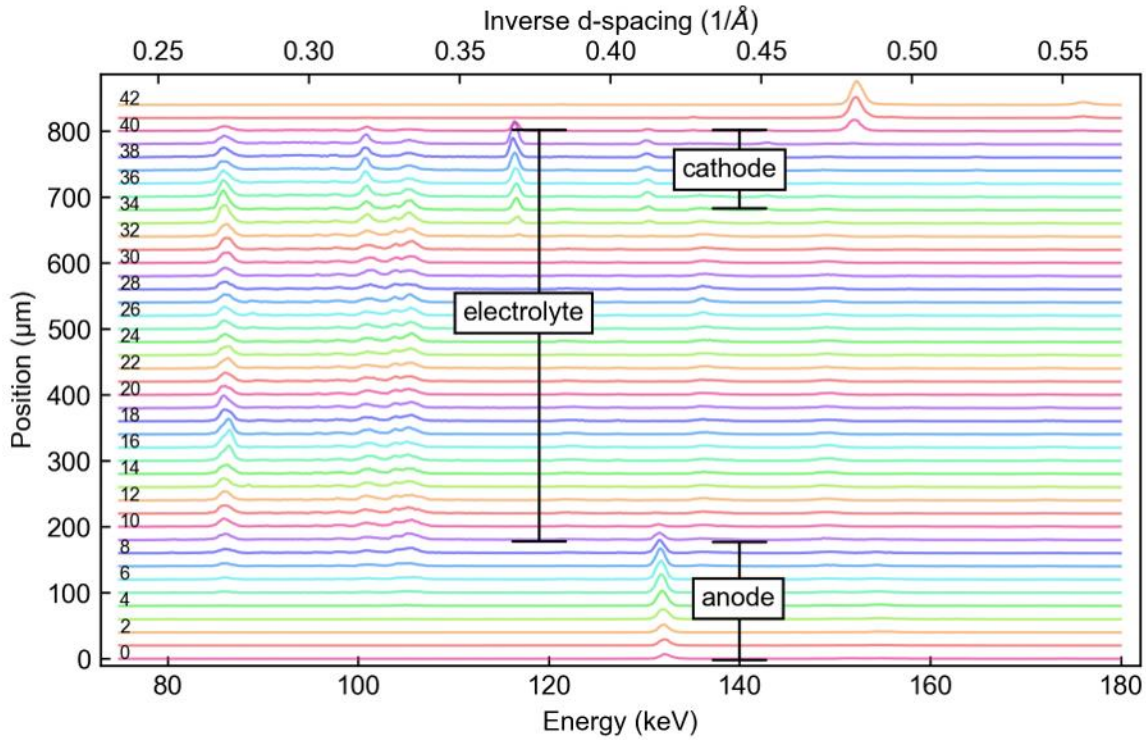

Figure S12. *Initial EDXRD data of pristine FeS_2/C/ $Li_{6.6}Ge_{0.6}Sb_{0.4}S_5I$ | $Li_{6.6}Ge_{0.6}Sb_{0.4}S_5I$ | Li-In full cell at time 1. This data is the same as is plotted in Figure 5b, but here it is plotted as individual diffraction patterns.*

13. The $Li_{6.6}Ge_{0.6}Sb_{0.4}S_5I$ (220) peak at location 34 inside the FeS_2 cathode as a function of time.

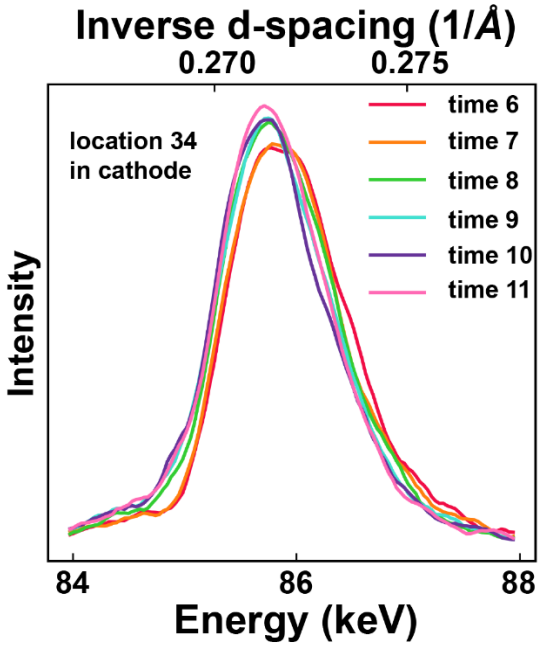

Figure S13. The $Li_{6.6}Ge_{0.6}Sb_{0.4}S_5I$ (220) peak at location 34 inside the FeS_2 cathode as a function of time.

Figure S14. SEM images of FeS_2/LGSSI/C electrodes before and after cycling.

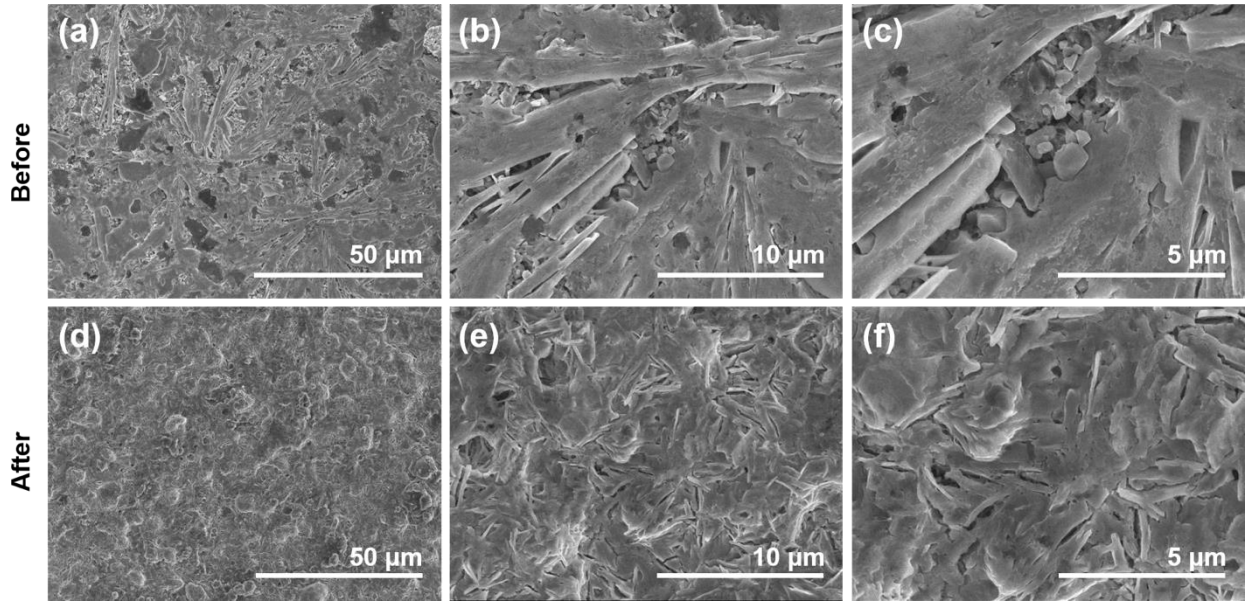

Figure S14*. Morphology evolution of FeS_2/LGSSI/C electrodes (a-c) before cycling and (d-e) after 220 cycling, with magnification of a) and d) 1k, b) and e) 5k, c) and f) 10k.*

Table S5. Performance comparison with reported ASLBs using FeS2 as cathode

ref	***Cathode***	***Electrolyte***	***Capacity***	***Cycle number***
This work	*FeS_2*	*$Li_{6.6}Ge_{0.6}Sb_{0.4}S_5I$*	*600 mAh/g at 90 mA/g*	*220*
3	*FeS_2*	*$Li_{10}GeP_2S_{12}$*	*197.1 mAh/g at 500 mA/g*	*100*
4	*FeS_2*	*$Li_{10}GeP_2S_{12}$*	*632.4 mAh/g at 30 mA/g*	*20*
	FeS_2		*171.1 mAh/g at 1000 mA/g*	*200*
5	*FeS_2*	*$77.5Li_2S$-$22.5P_2S_5$*	*~150 mAh/g at 500 mA/g*	*500*

[6]	FeS_2	$77.5Li_2S$-$22.5P_2S_5$	*750 mAh/g, at 92 mA/g*	*20*

1. Zhou, L.; Assoud, A.; Zhang, Q.; Wu, X.; Nazar, L. F., New Family of Argyrodite Thioantimonate Lithium Superionic Conductors. *Journal of the American Chemical Society* **2019,** *141* (48), 19002-19013.
2. Liu, H.; Liu, H.; Lapidus, S. H.; Meng, Y. S.; Chupas, P. J.; Chapman, K. W., Sensitivity and Limitations of Structures from X-ray and Neutron-Based Diffraction Analyses of Transition Metal Oxide Lithium-Battery Electrodes. *Journal of The Electrochemical Society* **2017,** *164* (9), A1802-A1811.
3. Wan, H.; Liu, G.; Li, Y.; Weng, W.; Mwizerwa, J. P.; Tian, Z.; Chen, L.; Yao, X., Transitional Metal Catalytic Pyrite Cathode Enables Ultrastable Four-Electron-Based All-Solid-State Lithium Batteries. *ACS Nano* **2019,** *13* (8), 9551-9560.
4. Mwizerwa, J. P.; Zhang, Q.; Han, F.; Wan, H.; Cai, L.; Wang, C.; Yao, X., Sulfur-Embedded FeS2 as a High-Performance Cathode for Room Temperature All-Solid-State Lithium–Sulfur Batteries. *ACS Applied Materials & Interfaces* **2020,** *12* (16), 18519-18525.
5. Whiteley, J. M.; Hafner, S.; Han, S. S.; Kim, S. C.; Oh, K. H.; Lee, S.-H., FeS2-Imbedded Mixed Conducting Matrix as a Solid Battery Cathode. *Advanced Energy Materials* **2016,** *6* (15), 1600495.
6. Yersak, T. A.; Macpherson, H. A.; Kim, S. C.; Le, V.-D.; Kang, C. S.; Son, S.-B.; Kim, Y.-H.; Trevey, J. E.; Oh, K. H.; Stoldt, C.; Lee, S.-H., Solid State Enabled Reversible Four Electron Storage. *Advanced Energy Materials* **2013,** *3* (1), 120-127.